Atmospheric
Chemistry
and Physics

Relation between total vertical column density and near-surface NO$_2$ based on in situ and Pandora ground-based remote sensing observations

Ying Zhang[1,2], **Yuanyuan Wei**[3], **Gerrit de Leeuw**[1,4], **Ouyang Liu**[1,2], **Yu Chen**[5], **Yang Lv**[1], **Yuanxun Zhang**[2], and **Zhengqiang Li**[1,2]

[1]State Key Laboratory of Remote Sensing and Digital Earth, Aerospace Information Research Institute, Chinese Academy of Sciences, Beijing 100101, China
[2]College of Resources and Environment, University of Chinese Academy of Sciences, Beijing 100049, China
[3]Changcheng Institute of Metrology & Measurement, Beijing 100095, China
[4]R&D Satellite Observations, Royal Netherlands Meteorological Institute (KNMI), 3730AE De Bilt, the Netherlands
[5]CMA Public Meteorological Service Centre, Beijing 100081, China

Correspondence: Yuanyuan Wei (weiyy020@avic.com)

Abstract. Nitrogen dioxide (NO$_2$) is a major pollutant that at high concentrations may affect human health. It is also a photochemically reactive gas that is important for the oxidation potential of the atmosphere and acts as a precursor for the formation of aerosol particles and ozone. However, monitoring of near-surface (NS) NO$_2$ faces the challenge of spatial discontinuity due to large distances between ground-based monitoring stations, whereas satellite remote sensing provides total vertical column density (VCD) that is related to near-surface (NS) concentrations in a complicated manner. In this study, the relation between total VCD and NS concentrations of NO$_2$ was analyzed based on total VCD from remote sensing observations using a ground-based Pandora spectrometer and NS NO$_2$ concentrations from in situ observations. Both instruments were located at the Beijing-RADI site (Beijing, China) during January 2022. The ratio between total VCD and NS NO$_2$ concentrations varies throughout the day with substantially different relations in the morning and afternoon. During the night and morning, the atmosphere was vertically stratified, with disconnected layers that prevented vertical mixing of atmospheric constituents. In the afternoon, these layers connected, allowing for vertical mixing and transport between the surface and the top of the boundary layer. Thus, the prohibition of vertical transport in the morning and the mixing in the afternoon resulted in different relations between the total VCD and NS NO$_2$ concentrations. These different relationships have consequences for the use of satellite remote sensing to estimate NS NO$_2$ concentrations.

1 Introduction

Nitrogen dioxide (NO$_2$) can have adverse effects on human health (Eum et al., 2022, 2019; Nordeide Kuiper et al., 2021; Kornartit et al., 2010). NO$_2$ plays an important role in atmospheric chemistry and acts as a precursor for the formation of ozone and secondary aerosols in the atmosphere. The major sources of NO$_2$ are fossil fuel burning, such as power plants, traffic, and households. Because of these anthropogenic sources, together with the relatively short atmospheric lifetime of NO$_2$, high tropospheric NO$_2$ concentrations are usually observed near highly industrialized regions (van der A et al., 2006), densely populated agglomerations (de Souza et al., 2022), and power plants (Tang et al., 2024), as well as along major highways (Goldberg et al., 2021) and shipping lanes (Ding et al., 2018). In addition, NO$_2$ is produced from some natural sources such as lightning and soil emissions.

Concentrations of NO$_2$ in the atmosphere can be measured using satellite-based sensors providing total and tropospheric column densities, ground-based remote sensing using MAX-DOAS or Pandora instruments, or in situ instruments. Satellite remote sensing is currently a widely used technique, for example, using the Ozone Monitoring Instrument (OMI, Levelt et al., 2006) on the Aura satellite and the TROPOspheric Monitoring Instrument (TROPOMI, Veefkind et al., 2012) on the Sentinel-5 Precursor (S5P) satellite. Satellite data show that the total vertical column density (VCD) of NO$_2$ is highly variable in space and time (e.g., Lamsal et al., 2014; Fan et al., 2021). Duncan et al. (2016) analyzed global NO$_2$ observed by OMI from 2005 to 2014 and found that NO$_2$ levels were initially high over China but had significantly decreased over the Beijing, Shanghai, and the Pearl River Delta (PRD) regions in 2014, in response to pollution control measures. In particular, over the PRD region, the NO$_2$ concentrations decreased by about 40 %. Also, in the following years, the NO$_2$ concentrations over China have substantially diminished in response to the implementation of emission reduction policy (e.g., van der A et al., 2017; Fan et al., 2021; de Leeuw et al., 2021) and fell below the 2008 level in 2017 (Zhao et al., 2023). However, the decrease seems to have flattened in recent years (Fan et al., 2021).

The Pandonia Global Network (PGN) of Pandora Spectrometer Instruments was established in 2018 (http://www.pandonia-global-network.org/, last access: 10 July 2024) to provide "quality observations of total column and vertically resolved concentrations of a range of trace gases". The PGN data are used, for instance, for the validation of products from environmental satellites. However, the comparison of OMI total VCD of NO$_2$ with Pandora observations at six sites in South Korea and the USA by Herman et al. (2019) showed that the mean and daily Pandora NO$_2$ concentrations were 50 % or more higher than those retrieved from OMI at sites that were frequently contaminated, such as Seoul, Busan, and Washington, DC. Tzortziou et al. (2018)

reported that Pandora total VCD of NO$_2$ during the KORUS-AQ coastal cruise experiment (Tzortziou, et al., 2015) was 10 %–50 % higher than OMI-derived total VCD of NO$_2$. The relationship between total VCD and near-surface (NS) concentrations of NO$_2$ was complex according to the analysis of data from the DISCOVER-AQ campaign in the Baltimore–Washington region in July 2011; the discrepancies were suggested to be caused by the large field of view of OMI (Flynn et al., 2014; Knepp et al., 2015; Reed et al., 2015; Tzortziou et al., 2015). Preliminary validation of total VCD of NO$_2$ from the Ozone Mapping and Profiler Suite (OMPS) aboard the joint NASA/NOAA Suomi National Polar-orbiting Partnership (Suomi NPP) satellite by Huang et al. (2022) in the USA showed that OMPS total VCD of NO$_2$ tends to be lower in polluted urban areas and higher in clean areas/events than Pandora observations. Ialongo et al. (2020) and Zhao et al. (2020) obtained similar results from the validation of TROPOMI total VCD of NO$_2$ using PGN data, but the differences were significantly smaller than those for the OMI and OMPS data with a coarser spatial resolution than TROPOMI. The validation of TROPOMI total VCD versus Pandora data at the Beijing-RADI site shows the good performance of TROPOMI (Liu et al., 2024). It is noted that Liu et al. (2024) resampled the TROPOMI data to a spatial resolution of $100 \times 100\,\mathrm{m}^2$, i.e., similar to that of the Pandora observation area.

Satellite-derived total VCD of NO$_2$ data are often used to determine trends (e.g., van der A et al., 2017; Fan et al., 2021) but, in view of the above, the relation between total VCD and NS concentrations of NO$_2$ is more complex. For instance, Fan et al. (2021) discussed the total VCD/NS relationship for selected major urban regions in China during the first 20 weeks after the COVID-19 lockdown and observed substantial differences (their Fig. 9). Chang et al. (2022) analyzed data from the Geostationary Environment Monitoring Spectrometer (GEMS) Map of Air Pollution (GMAP) campaign conducted during 2020–2021. Their results indicate that total VCD and NS concentrations of NO$_2$ exhibit a stronger correlation under advective boundary layer conditions at high wind speeds, where the vertical distribution of NO$_2$ is more uniform. In contrast, the presence of plumes from large point sources, either decoupled from the surface or transported from nearby cities, enhances the vertical heterogeneity of NO$_2$. These plumes contribute to a less consistent relationship between total VCD and NS concentrations of NO$_2$. Similarly, Liu et al. (2024) showed different relations between total VCD and NS concentrations of NO$_2$ for low and high concentrations, which are qualitatively explained in terms of transport and local emissions. Moreover, Thompson et al. (2019), using data from the KORUS-AQ coastal cruise experiment, reported that there is no consistent correlation between total VCD and NS concentrations of NO$_2$ across different cases and that the relation between total VCD and NS concentrations of NO$_2$ is complex. Thus,

to accurately assess NO$_2$ pollution in China and its effects on air quality, accurate ground-based observations are needed.

Although a large number of ground-based NO$_2$ observation stations have been established in China since 2012 by the China National Environmental Monitoring Center (CNEMC) of the Ministry of Ecology and Environment of China (MEE) for the provision of the ground-based monitoring data (available at http://www.mee.gov.cn/, last access: 8 July 2024), there are still large areas for which no data are available. Satellite data can fill these gaps by converting satellite observations of aerosols and trace gases from total VCD and NS concentrations. Such data are usually provided by sensors flying on polar-orbiting satellites with global coverage but with a single overpass per day, which at most latitudes cannot provide the daily variability of NO$_2$ characteristics. However, with the launch of geostationary satellites, spatial and temporal distributions of NO$_2$ concentrations can be obtained within the satellite field of view throughout the day. The GEO-KOMPSAT-2B geostationary satellite, launched by the National Institute of Environmental Research (NIER) under the Ministry of Environment, South Korea, in February 2020, carries the Geostationary Environment Monitoring Spectrometer (GEMS), which provides high-resolution measurements of total VCD of key air quality components (Kim et al., 2020). With the launch of GEMS, the Asian region was the first to achieve coordinated hour-by-hour monitoring of pollutants. GEMS will form a constellation of satellites to monitor air quality globally with high temporal and spatial resolution, together with the Tropospheric Emissions: Monitoring Pollution (TEMPO) mission, launched by NASA on 7 April 2023 to cover the North American region (https://tempo.si.edu/overview.html, last access: 18 April 2025) and Sentinel-4, planned to be launched on the Meteosat Third Generation Sounder (MTG-S) by the European Organisation for the Exploitation of Meteorological Satellites (EUMETSAT) in 2025 (https://www.eumetsat.int/meteosat-third-generation-sounder-1-and-copernicus-sentinel-4, last access: 18 April 2025).

While geostationary satellites enable continuous daytime observations of total VCD of NO$_2$, discrepancies between total VCD and NS concentrations of NO$_2$ remain a critical challenge. The weak correlation between NS NO$_2$ concentrations and satellite-derived total VCD of NO$_2$ (Lamsal et al., 2014) is closely tied to differences in their vertical distribution, atmospheric lifetimes, and chemical reaction pathways (Xing et al., 2017). Despite extensive efforts to derive NS NO$_2$ concentrations from total VCD measurements (Chang et al., 2025; Wei et al., 2022; Zhang et al., 2022; Dou et al., 2021), the dynamic complexity of the planetary boundary layer introduces substantial uncertainties. Moreover, prior studies have emphasized the roles of vertical NO$_2$ distribution (Sun et al., 2023; Zhang et al., 2023; Kang et al., 2021) and regional pollutant transport contributions (Yin et al., 2025; Dong et al., 2020; Chang et al., 2019; Li et al., 2017), but research explicitly linking regional transport

processes to vertical NO$_2$ concentration gradients and elucidating their interactive effects remains limited. Song et al. (2024) obtained NS NO$_2$ concentrations based on the Himawari-8 geostationary satellite using machine learning, which showed good performance in the noon and afternoon and relatively poor performance in the morning. These knowledge gaps are further exacerbated by satellite data limitations in resolving NS pollution, which has direct implications for human health assessments. To address these challenges, we need to integrate ground-based remote sensing observations with in situ NS NO$_2$ measurements to investigate vertical decoupling phenomena and the influence of distinct pollutant transport pathways on NS NO$_2$ pollution dynamics.

The first operational Pandora instrument in China was installed at the Beijing-RADI site in 2021, for the ground-based remote sensing of several trace gases, including NO$_2$. The Beijing-RADI Pandora instrument is part of the PGN network, and all data are publicly available via the PGN website (https://data.pandonia-global-network.org/Beijing-RADI/Pandora171s1/, last access: 22 January 2025) within 1 d of the observations. The aim of this study is to analyze the relationship between total VCD of NO$_2$ obtained by remote sensing and NS measurements during a field experiment at the Beijing-RADI site during 10–29 January 2022. In order to better determine and understand the relation between total VCD and NS concentrations of NO$_2$, we also used auxiliary data such as simultaneous measurements of PM$_{2.5}$ mass concentrations, lidar observations, meteorological parameters, and satellite observations. Section 2 presents the experiments and data, Sect. 3 presents the main results, and the conclusions and discussion are presented in Sect. 4.

2 Materials and method

2.1 Site description

Beijing is a metropolis with an area of 16 800 km^2 and a population of nearly 22 million (2023) (https://worldpopulationreview.com/world-cities/beijing-population, last access: 22 January 2025). High mountains are located to the north and west of Beijing (Fig. 1). The rapid economic development of Beijing and the topography of the area lead to the emission of pollutants that may either disperse or accumulate, depending on wind direction and wind speed. During northwesterly winds, clean air is transported from the mountains, whereas during southerly winds, polluted air is transported from the highly industrialized North China Plain. The southerly airflow is blocked by the mountains to the west and north, and thus pollution accumulates, in particular, during certain weather conditions conducive to the formation of smog, such as low wind speed. Photochemical processes may further contribute to the build-up of pollution that may result in the formation of haze.
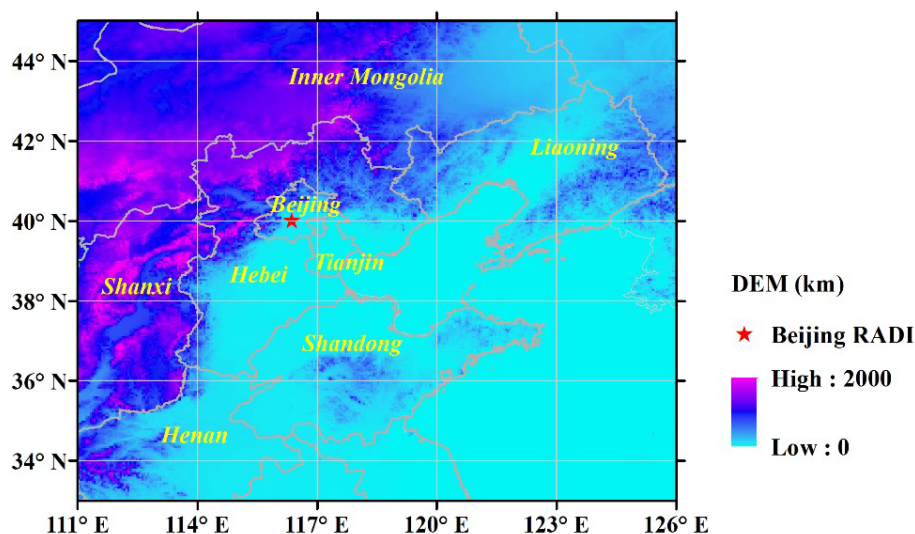
Figure 1. Digital elevation map of the study area showing the location of the Beijing-RADI site (40.004° N, 116.379° E, altitude at 59 m) (red star) and surrounding mountains.

The Beijing-RADI site is located on the roof (22 m above the surface) of the Aerospace Information Research Institute of the Chinese Academy of Sciences (40.004° N, 116.379° E, elevation 59 m), which in turn is located in the north of Beijing between the Fourth and Fifth Ring Roads at the edge of the Olympic Park. The site is representative of an urban background affected by vehicle exhaust, combustion, and domestic emissions, including those from heating during wintertime.

A short-term field experiment was carried out at the Beijing-RADI long-term observation site during 10–29 January 2022. Pandora provided total VCD of NO$_2$ concentrations in four layers; information on the spatial distribution of total VCD of NO$_2$ was obtained from TROPOMI; and a lidar provided aerosol backscatter profiles, showing the vertical structure and evolution of the atmospheric boundary layer. The NS parameters were measured with instrumentation mounted near the Pandora on the roof of the AirCAS building, as described in the following sections.

2.2 Observations of column-integrated parameters and vertical profiles

2.2.1 Pandora

Pandora is a UV-visible spectrometer that can provide high-quality measurements of spectrally resolved direct-sun/lunar or sky scan radiances. It uses direct solar measurements to obtain total VCD of NO$_2$ and sky measurements to obtain the vertical layer concentrations of NO$_2$, with a field of view of 2.6° in direct-sun mode and 1.5° in sky mode (Cede, 2024). Based on the Beer–Bouguer–Lambert law, the spectra observed at 400–470 nm in direct-sun mode are used to invert total VCD of NO$_2$ using the differential optical absorption

spectroscopy (DOAS) technique of trace gas spectral fitting. Pandora's direct-sun measurements depend only on the geographic location with a known solar zenith angle, which simplifies the air mass factor for correction of the atmospheric light path (Chang et al., 2022). Pandora measures total VCD of NO$_2$ with a clear-sky precision of 0.01 DU and a nominal accuracy of 0.1 DU (Herman et al., 2009). In view of this high precision, we use total VCD of NO$_2$ from the nvs3 product in this study and select data with a quality control flag of L10. Diffuse (scattered) radiation is measured at five pointing zenith angles (PZAs) in sky mode that, together with the direct sun measurement, provides information on the tropospheric VCD and on the surface concentrations. The PZAs are 0, 60, 75, 88°, and the maximum angle taken was 89°. The measurements are taken in a V shape (all angles are measured twice around a central angle), as described in Cede (2024). Four partial columns of NO$_2$ concentrations are provided by the Pandora inversion. The first step is the estimation of the effective height corresponding to a given PZA and then the calculation of differential air mass factors for the NO$_2$ and the air gas for each layer. The profile shape of the partial columns is determined as a variation of the air-gas shape. The average number density of the NO$_2$ in each layer is then calculated. The partial column amounts can be obtained from the concentrations multiplied by the layer width as described in the Manual for Blick Software Suite (Cede, 2024), Sect. 6.7. The NO$_2$ of the partial column can be obtained from the uvh3 product, which was downloaded from the PGN website (https://pandonia-global-network.org, last access: 22 January 2025). We converted these partial column concentrations into layer-averaged volume mixing ratios and interpolated them to six standard levels (0.2, 0.5, 1.0, 1.5, 2.0, and 2.5 km) for visualization.

2.2.2 Lidar

A small lidar developed by the Hefei Institute of Physical Sciences, Chinese Academy of Sciences, was used for continuous measurements of aerosol backscatter profiles during day and night. The GBQ L-01 aerosol lidar consists of a laser, optical unit, control unit board, high-speed signal acquisition card, industrial motherboard, and communication module. The GBQ L-01 aerosol lidar uses a high-frequency pulse laser emitting linearly polarized light at a wavelength of 1064 nm. The optical unit consists of a transmitter and a receiver. The optical transmitter unit emits laser light pulses, which are expanded before they are emitted into the atmosphere. The optical receiver unit consists of a telescope that focuses the backscattered light onto an optical detector, which in turn is connected to an amplifier unit. The vertical and parallel polarized components of the backscattered light are separated by the polarizing prism in the receiving channel. The industrial motherboard carries lidar acquisition and control software and data analysis software to control the overall operation of the system.

2.2.3 TROPOMI

The TROPOMI (TROPOspheric Monitoring Instrument) is a passive-sensing hyperspectral nadir-viewing imager aboard the Sentinel-5 Precursor (S5P) satellite, launched on 13 October 2017. S5P flies at an altitude of 817 km in a near-polar sun-synchronous orbit. The local Equator overpass time in the ascending node is 13:30, and the repetition period is 17 d (KNMI, 2017). TROPOMI's four separate spectrometers cover wavelengths in the ultraviolet (UV), UV–visible (UV–VIS), near-infrared (NIR), and short-wavelength infrared (SWIR) spectral bands (Veefkind et al., 2012). The NO$_2$ used in this study is derived from spectral measurements of solar radiation in TROPOMI's UV–VIS wavelength bands (van Geffen et al., 2015, 2019). Compared to the relatively small field of view of the Pandora instrument, the size of the TROPOMI ground pixel (3.5 km × 5.5 × km; across × along track) is relatively large. In addition, only tropospheric vertical column densities (VCDs) for NO$_2$ were available during the time period of this study. The TROPOMI tropospheric VCDs for NO$_2$ are only used as a qualitative reference for upwind concentrations in the evaluation of effects of long-range transport using air mass backward trajectories and not for quantitative analysis. Furthermore, tropospheric NO$_2$ column densities are used because these are more representative of near-surface NO$_2$.

2.3 Near-surface measurement

2.3.1 Trace gas analyzer

The Thermo Fisher Scientific Model 42i Trace Level Chemiluminescence NO-NO$_2$-NO$_x$ Analyzer (https://cires1.colorado.edu/jimenez-group/Manuals/

Manual_NOx_42i.pdf, last access: 22 January 2025) was used to measure NS NO$_2$ concentrations. This instrument first transforms NO$_2$ into nitric oxide (NO) using a molybdenum NO$_2$ to NO converter heated to about 325 °C. Then, NO and ozone (O$_3$) react to produce a characteristic luminescence with an intensity linearly proportional to the NO concentration (Thermo Fisher Scientific, 2007). NO$_2$ values are derived by subtracting NO from NO$_x$ measurements. Measurements were made every minute during the observation period.

2.3.2 Beta attenuation monitor

Ground-based near-surface PM$_{2.5}$ concentrations were measured using the beta attenuation monitor Met One BAM-102 equipped with a PM$_{2.5}$ inlet. The Met One BAM-1020 collects aerosol particles on glass filter tape. PM$_{2.5}$ is measured using beta rays generated by a small ^{14}C source (https://metone.com/products/bam-1020/, last access: 18 April 2025). At the start of every measurement cycle, the flux of beta rays is measured across clean filter tape to determine a zero reading. Next, the filter tape is advanced and ambient air is sampled at the same spot, with a controlled airflow, thereby impregnating the tape with PM$_{2.5}$. After the sampling is completed, the tape retracts and PM$_{2.5}$ samples are dried (in an environment with relative humidity lower than 40 %, which removes most of the water content) by a built-in heater. Then the concentration of PM$_{2.5}$ collected on the filter tape is measured as described above. Samples are taken every hour.

2.3.3 Auxiliary meteorological data

In addition to the above observations, we also use weather maps, meteorological surface observations, and sounding observations published by the World Meteorological Organization (WMO) to aid in our analyses. Weather maps for the Asian region are published by the Korea Meteorological Administration and can be downloaded at http://222.195.136.24/chart/kma/data_keep (last access: 22 January 2025). We downloaded the surface and sounding observations of the meteorological station 54511 in Beijing, located at 39.93° N, 116.28° E, which is part of the WMO network. These data are available from the website of the University of Wyoming (http://weather.uwyo.edu/surface/, last access: 22 January 2025). Although this station is far away from our experimental site (about 23 km), it is representative of the macroscopic changes of the meteorological conditions in Beijing.

2.4 HYSPLIT model

To better understand the regional transport pathways and source regions at different altitudes, backward trajectories from the Hybrid Single Particle Lagrangian Integrated Trajectory (HYSPLIT; Draxler and Hess, 1998) model were

used. The HYSPLIT model assumes that the parcel trajectory is formed through time integration and spatial differences while moving in the wind field. The path of the air mass is mainly related to the airflow situation, pressure system movement, and topography (Draxler and Hess, 1998). The HYSPLIT model has the ability to deal with a variety of meteorological input fields and physical processes and can also be used to describe atmospheric transport, diffusion, and deposition of pollutants and harmful substances (Stein et al., 2015). In this study, the backward trajectories were initialized for arrival at the Beijing-RADI site at 300, 500, and 1000 m. The HYSPLIT model was run at https://www.ready.noaa.gov/HYSPLIT_traj.php (last access: 18 April 2025), with the input meteorological field data (0.25° × 0.25°) provided by the Global Forecasting System.

3   Results and analysis

3.1   Data overview

Time series of the measured NS and total VCD of NO$_2$ during the study period are presented in Fig. 2a. For comparison of NS NO$_2$ concentrations with Pandora observations, they are expressed in mg m^{-3}. Figure 2a shows the common diurnal variation of the NO$_2$ concentrations, i.e., a gradual decrease in the morning to a minimum around mid-day, followed by a gradual increase in the afternoon to a maximum value during the night. This diurnal variation is due to photochemical reactions during daytime, meteorological effects, and anthropogenic emissions during certain hours (for instance, during rush hour) (e.g., Atkinson, 2000; Boersma et al., 2009; Zhang et al., 2016; Cheng et al., 2018; Li et al., 2021). Total VCD of NO$_2$ concentrations can only be measured with Pandora during daytime. The diurnal variations between 08:00 and 16:00 local Beijing time (UTC+8; throughout this paper local time, LT, will be used) at the Beijing-RADI site are similar to those of NS NO$_2$. Based on the variation of the NS NO$_2$ concentrations (Fig. 2a), three periods are considered during the study period: Period I: 10 to 18 January, with strong diurnal variations and high NO$_2$ concentration peaks; Period II: 19 to 24 January, when NS NO$_2$ sharply decreases and then increases with stronger fluctuations, but total VCD of NO$_2$ is not available due to the presence of clouds; Period III: 25 to 30 January, when a sudden drop occurred on 25 January and low NO$_2$ concentrations with some narrow peaks lasted until the 30th.

The time series of the NS PM$_{2.5}$ concentrations in Fig. 2b shows four peaks in Period I, with maximum values during the night and very low concentrations ($< 10 \, \mu g \, m^{-3}$) during daytime. The maxima were relatively low on 12 and 17 January ($\sim 25 \, \mu g \, m^{-3}$), whereas on 14 and 18 January the PM$_{2.5}$ peak concentrations were ~ 120 and $\sim 70 \, \mu g \, m^{-3}$. During Period II, the PM$_{2.5}$ concentration increased steadily from less than $25 \, \mu g \, m^{-3}$ on 20 January to more than $125 \, \mu g \, m^{-3}$ on the 24th, with similar day/night variations as

in Period I. During Period III, the PM$_{2.5}$ concentrations were relatively low ($< 25 \, \mu g \, m^{-3}$), and there was no clear diurnal variation.

The air temperature and relative humidity (RH) during the study period are presented in Fig. 2c, and the wind speed and wind direction are presented in Fig. 2d. During Period I, air temperature, RH, and wind speed all varied strongly with a clear diurnal pattern: elevated wind speed during the day, with daily maxima between about 7 and 13 m s^{-1}, and very low wind speed during the night ($< 2 \, m \, s^{-1}$); daytime air temperatures around 0 °C and nighttime temperatures around -10 °C; dry air during the day (RH ~ 20 %) and more humid during the night (RH of 60 %–80 %). The wind was mostly from northerly directions (NW–NE) and veering during the night. During Period II, the air temperature increased gradually from about -5 to about 0 °C, with small diurnal variations, and relative humidity (RH) increased initially from 40 % to 60 % on 20 January and then gradually to about 70 %, with little day/night variations. During the nights of 22–25 January, the humidity was very high, and the RH sensor saturated and reported maxima close to 100 %. Wind speed during this period was low ($< 3 \, m \, s^{-1}$), and wind direction was mostly SE. During Period III, day/night temperature and RH fluctuations occurred, with daytime air temperatures above 0 °C and gradually rising and RH varying between 20 % during the day and 60 % during the night. Wind speeds were higher during the day, mostly a little higher than 3 m s^{-1}, than they were during the night (close to 0 m s^{-1}), and wind direction was mostly northerly.

The variations of the NO$_2$ and PM$_{2.5}$ concentrations were similar in the sense that the minimum and maximum peak concentrations occurred at about the same time, but with differences in the ratios between minima and maxima. The occurrence of peak concentrations during the night is consistent with the variation in meteorological conditions, with maxima during low wind speed and low air temperature, conducive to the formation of a nocturnal boundary layer in which the concentrations accumulate near the surface. This is observed during Periods I and III. During Period II, however, there were no Pandora observations during daytime due to the occurrence of clouds. This suggests that clouds may also have been present during the night. Hence, radiative cooling was reduced, and air temperature did not decrease as much as during the other periods. Wind speed was low, so pollutants were not transported away and accumulated in the area, as also indicated by the high RH. Hence, the concentrations of NO$_2$ and PM$_{2.5}$, as well as RH, gradually increased during Period II, with relatively small diurnal variations.

For further analysis, we selected two cases for which both total VCD and NS concentrations of NO$_2$ data were available, including lidar observations and air mass trajectories. The selected cases are the periods when both NO$_2$ and PM$_{2.5}$ concentrations were high, i.e., on 14 and 18 January, when the 24 h average NO$_2$ concentrations exceeded 80 mg m^{-3}. The first pollution episode (case 1) started in the afternoon
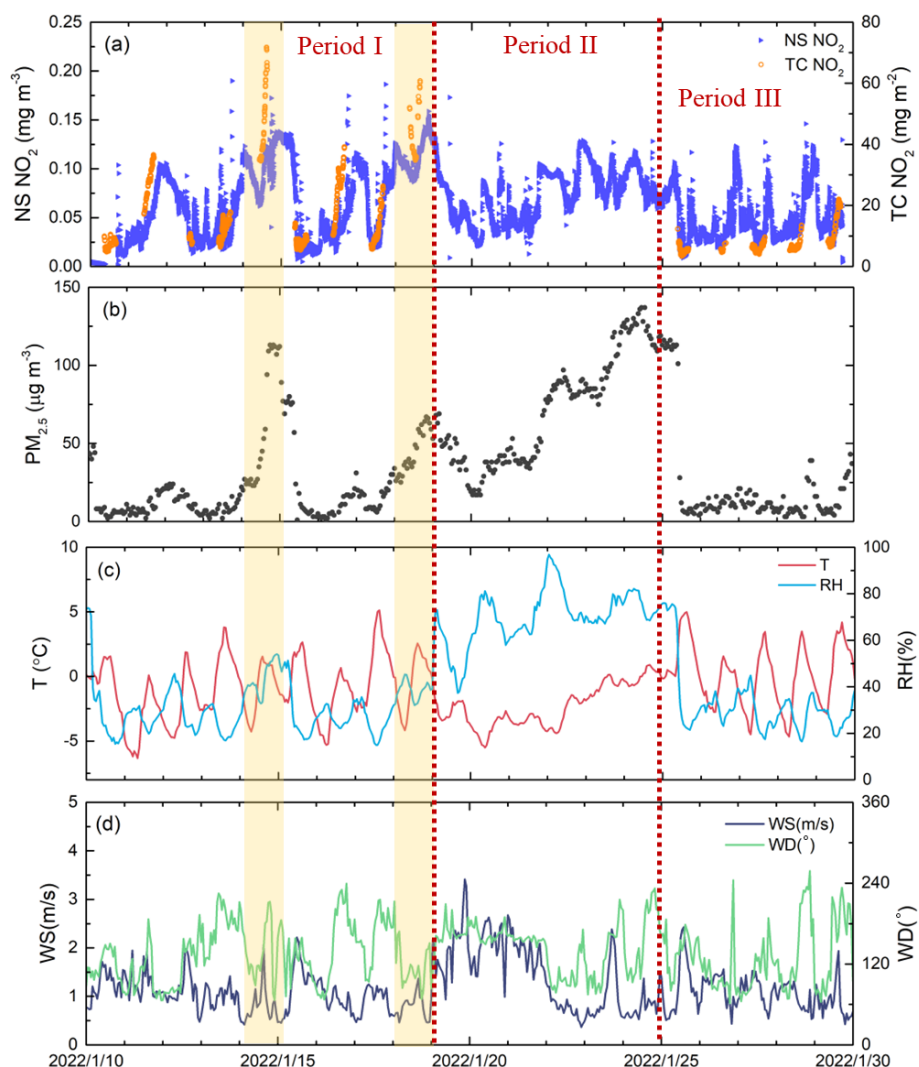
Figure 2. Time series of observed parameters from 10 to 29 January 2022, **(a)** total VCD and NS concentrations of NO$_2$, **(b)** NS PM$_{2.5}$ concentration, **(c)** temperature and relative humidity, and **(d)** wind speed and wind direction from WMO meteorological station 54511 in Beijing. The vertical dotted lines mark the boundaries between the three periods, and the yellow shaded rectangles mark the two cases discussed in Sect. 3.2.

of 14 January and ended in the morning of 15 January. The other pollution episode with high NS NO$_2$ occurred on 18 January (case 2). The diurnal variation of the NS NO$_2$ concentrations was similar in both cases, while the air temperature, RH, wind speed, and wind direction showed that the meteorological situations were similar. However, differences are observed in the temporal variations of total VCD of NO$_2$ concentrations versus NS NO$_2$ concentrations and in PM$_{2.5}$ concentrations.

3.2 Variations of total VCD and NS concentrations of NO$_2$ during the two selected cases

Many studies (Yin et al., 2025; Dong et al., 2020; Chang et al., 2019; Li et al., 2017) indicated that the pollution in Beijing mainly originates from three pollution transport patterns: southwest (SW), southeast (SE), and south mixing (SM) patterns. Among them, the most representative are the SW transport path from Shanxi Province to Shijiazhuang–Baoding–Beijing and the SE transport path from Shandong province to Cangzhou–Langfang–Tianjin–Beijing. However, few studies have explored the vertical transport of pollution types. Cases 1 and 2 are representative of the widespread SW and SE patterns, respectively. The processes influencing the concentrations are identified based on lidar data, providing information on the boundary layer structure, together

with large-scale weather maps and air mass trajectory analyses, providing information on sources of pollutants and their transport over a wider area. Our study primarily focuses on the correlation between total VCD and NS concentrations of NO$_2$. Total VCD of NO$_2$ is provided by the passive remote sensing instrument Pandora, which does not provide reliable observations on cloudy days, as mentioned above. This is the reason why we only selected cases during Period I and did not obtain cases during Period II, when pollution was more severe.

3.2.1 Case 1: disconnected boundary layers merging (14 January 2022)

Time series of the total VCD and NS concentrations of NO$_2$ on 14 January 2022 (Fig. 3a) show their different evolution throughout the day. NS concentrations showed diurnal variation, decreasing from midnight (0.11 mg m^{-3}) to the morning (0.065 mg m^{-3} at 10:30), followed by an afternoon increase and strong evening fluctuations (0.04–0.175 mg m^{-3}), likely associated with rush hour emissions and domestic heating. During the limited observation window (10:30–15:30) for Pandora, both VCD and NS concentrations initially showed similar behavior with minimal variation. However, their temporal patterns diverged after 13:00, while NS concentrations plateaued, VCD exhibited rapid growth (40 to 72 mg m^{-2} between 12:00 and 15:00), nearly doubling before declining slightly. The difference in the temporal behavior between the total VCD and NS concentrations of NO$_2$ is amplified in Fig. 3b, which shows a scatterplot between the total VCD and NS concentrations. Observations before and after 13:00 are plotted with different symbols and are color coded in blue and red, respectively. For each of these two data sets, before and after 13:00, VCD and NS concentrations are well correlated with linear correlation coefficients R of 0.94 and 0.85, respectively, but with significantly different slopes.

The different behavior of the total VCD and NS concentrations of NO$_2$ can be explained by considering the dynamical behavior of the boundary layer structure. Lidar observations reveal the vertical structure of the atmospheric boundary layer from the variation of the lidar signal as a function of height. A 3-D plot of the vertical variation of the lidar signal, measured on 14 January 2022 at the Beijing-RADI site, close to the Pandora and the ground-based measurements, is presented in Fig. 3c. The lidar signals are color coded according to the scale to the right of Fig. 3c, and each vertical line shows the variation of the lidar signal with height, plotted along the primary vertical axis. The time of measurement of each profile is plotted along the horizontal axis. The lidar signal in this figure is range-corrected, i.e., corrected for attenuation as the laser light propagates in the atmosphere away from the emitter and, after backscattering by aerosol particles, back to the receiver. The time between emission of the laser pulse and receiving the backscattered signal is a measure of the height where the backscattering takes place

(after correction of the slant to a vertical optical path), and the intensity is a measure of the aerosol concentration.

The lidar observations in Fig. 3c revealed a complex boundary layer structure with distinct aerosol layers. The data show a well-mixed shallow boundary layer between midnight and 03:00 and the formation of an internal boundary layer after about 04:00, disconnected from the layer above. The internal boundary layer rises gradually until about 11:00 (up to about 400 m), with the clean layer above (between 400 and 500 m), and a new layer (at heights of approximately 800 to 900 m) appears around 07:00, probably due to advection. This vertical variation indicates a disconnected boundary structure with two disconnected layers, likely caused by nocturnal cooling (Stull, 1988). The temperature gradient prohibited material exchange between these layers, leading to the accumulation of near-surface emissions and the trapping of trace gases and aerosols in the upper layer. The occurrence of such a situation is consistent with the observations discussed in Sect. 3.1 and Fig. 2, with low wind speed, lowest air temperature during Period I (-12 °C), and enhanced RH (indicating trapping of water vapor together with decreased air temperature). Note that wind direction was southeasterly during a short period of time on 14 January with a wind speed of 2 m s^{-1}, slightly more than during the rest of the day when the wind direction was northerly. During southeasterly winds, polluted air may be advected to the Beijing-RADI site, whereas during northerly winds, clean air is advected (Liu et al., 2024).

The lidar data in Fig. 3c show that after 12:00, the lower layer deepened and backscatter was observed from the clean layer, indicating that aerosol was gradually mixed into that layer, which completely disappeared around 14:00. At the same time, the lidar signal from the growing lower layer increased gradually, whereas after 13:00 the lidar signal from the upper layer became smaller, indicating that the aerosol concentration decreased until both layers were mixed around 14:00 into a well-mixed boundary layer. After 15:00, the lidar signal increased, first near the surface and then growing throughout the boundary layer. The increase in the NS concentrations (Fig. 3a) is consistent with the highest PM$_{2.5}$ concentrations as presented in Fig. 2b and the overall increase in the lidar signal, indicating increasing aerosol concentrations. This is confirmed by AERONET aerosol optical depth (AOD) observations at the Beijing-RADI site (https://aeronet.gsfc.nasa.gov/cgi-bin/data_display_aod_v3?site=Beijing_RADI&nachal=2&level=2&place_code=10, last access: 18 April 2025), which, however, were only available until 16:00 LT.

The vertical variation of the NO$_2$ concentrations, derived from the Pandora sky radiance measurements at four elevations, is presented in Fig. 3d. Pandora data are only available during daytime, and therefore only the period from 08:00–16:30 can be shown. The NO$_2$ concentrations are available in four layers. Assuming that NO$_2$ is uniformly distributed within each layer, the data were interpolated to form a time
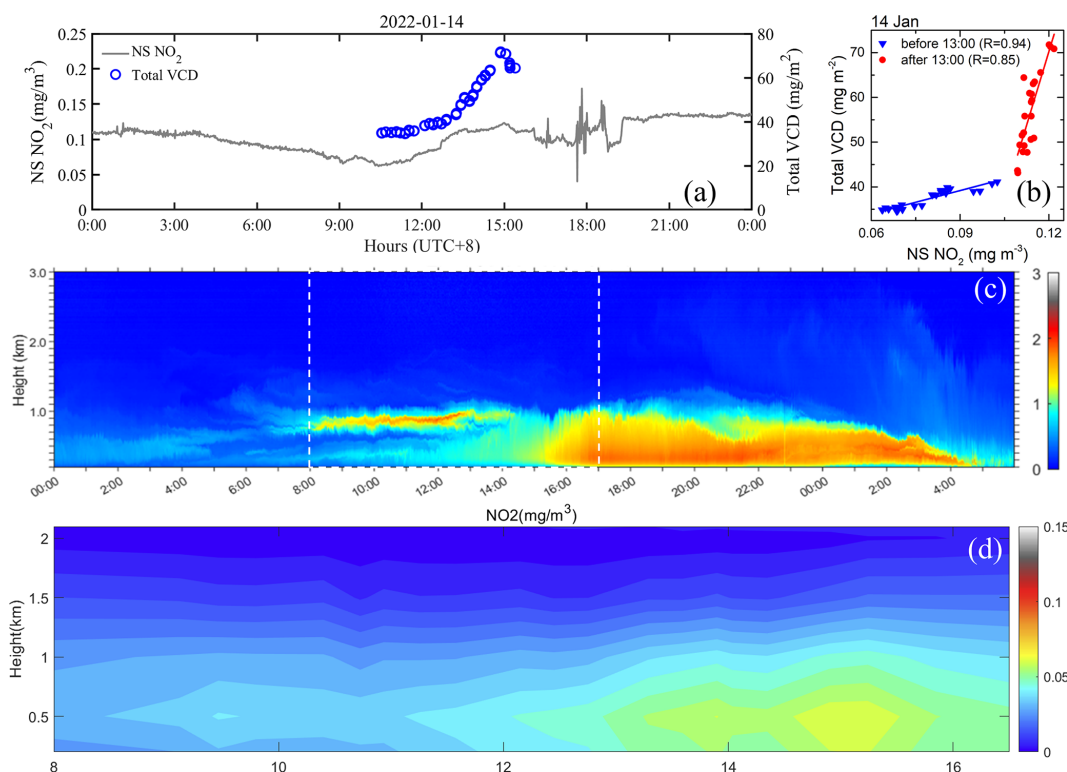
Figure 3. (a) Time series of NS NO$_2$ (gray line) and total VCD of NO$_2$ (blue circles) at the Beijing-RADI site (40.004° N, 116.379° E) on 14 January 2022; **(b)** scatterplots of total VCD and NS concentrations of NO$_2$ and fits to these data during the morning (before 13:00) and during the afternoon (after 13:00), showing different relationships as discussed in the text; **(c)** time series of vertical profiles of range-corrected lidar signals at 1064 nm. Note that the lowest height in panel **(c)** is 100 m; **(d)** time series of NO$_2$ vertical profiles derived from Pandora sky radiance measurements. Note that the Pandora profiles are constructed from layer-averaged volume mixing ratios interpolated to six standard levels, and the lowest level is 0.2 km.

series of NO$_2$ vertical distributions, similar to the lidar profiles. The data in Fig. 3d show the similar behavior of the NO$_2$ concentrations and the aerosol backscatter, with increasing concentrations between 12:00 and 17:00 and their vertical mixing. In particular, the increase around 15:00 is evident in both the Pandora and lidar observations. However, the Pandora observations do not show the occurrence of disconnected boundary layers in the morning. Instead, the Pandora observations show an enhanced layer between 300 and 800 m, rather than the more detailed structure visible in the lidar data. These differences stem from the difference in vertical resolution between the Pandora and the lidar: the total VCD from Pandora is divided into two layers (approximately 300–800 and 800–1700 m) within the detailed stratified height range (300–1000 m) observed by the lidar. Consequently, the fine stratified structure within 1000 m cannot be identified with the available Pandora data.

The overall similarity between the variations in the lidar and Pandora observations supports the use of lidar observations to explain the dynamic behavior of the NO$_2$ concentrations. In particular, the different relations between total VCD and NS observations before and after 13:00 (Fig. 3b) can be

explained by the occurrence of disconnected layers. The variations of the NS NO$_2$ concentrations until 13:00 reflect the effects of chemical processes and emissions within the atmospheric layer near the surface and within the elevated layer where only removal processes influence the NO$_2$ concentrations. As a result, the temporal variation of the concentrations in both layers was in part influenced by the same processes, differences were not large (Fig. 3a), and the relationship between the total VCD and NS concentrations was linear with a small slope (174.24) and a strong correlation ($R = 0.94$) (Fig. 3b). In the afternoon, such processes resulted in the increase in NO$_2$ concentrations, but when the two layers connected and the wind speed increased somewhat (Fig. 2c, d), NO$_2$ was mixed throughout the whole boundary layer up to about 1000 m. Hence, the usual afternoon increase in NO$_2$ concentrations near the surface (Liu et al., 2024) was offset by upward transport, distributing the NO$_2$ across the whole boundary layer and thus enhancing the total VCD. This is well illustrated by the time series of both NC and total VCD between 13:00 and 15:00 (see Fig. 3a). As a result, the relationship between total VCD and NS changed substantially after 13:00 (Fig. 3b).

The effect of transport on the NO$_2$ concentrations at the Beijing-RADI site on 14 January 2022 was analyzed using the data presented in Fig. 4: the spatial distribution of tropospheric NO$_2$ columns derived from TROPOMI data (overpass time 13:30), the synoptic weather map at 00:00 UTC, and 24 h backward trajectories for arrival at the Beijing-RADI site at altitudes of 300, 500, and 1000 m at 10:00, 13:00, and 16:00 LT. The TROPOMI data show the relatively high tropospheric NO$_2$ concentrations over the study area, in particular over an elongated area stretching from the SW to the NE over Hebei Province, including Beijing (compare with Fig. 1), and from Beijing eastward. This area is bounded by the Taihang mountains in the west and by the Yan mountains in the north, blocking transport of pollutants. The weather map in Fig. 4b shows the pressure distribution and location of low pressure areas resulting in wind from the SW, i.e., along the direction of the elongated area with elevated NO$_2$ concentrations (see Fig. 4a). This is confirmed by the air mass trajectories in Fig. 4c, all showing overall transport from the SW. However, the trajectories arriving at 10:00 LT show that, during the last 8 h, the air mass arriving at 300 m came from the NE at low wind speed, and the air mass arriving at 500 m came from the NW at even lower wind speed. The air mass arriving at 1000 m came from the SW during the last 14 h before arrival and from the NW during the earlier 12 h. The air masses arriving at 13:00 show similar trajectories. These trajectories are consistent with the lidar observation of disconnected layers, with different air mass trajectories during the last hours before arriving at the Beijing-RADI site and thus possibly different compositions. The air mass arriving at 1000 m had been at high elevations during its entire 24 h trajectory and originated from altitudes higher than 1500 m, but those arriving at 300 and 500 m originated from the surface at different locations separated by tens of km and may thus have been influenced by different sources.

3.2.2   Case 2: multi-layer structure on 18 January 2022

Time series of the total VCD and NS concentrations of NO$_2$ on 18 January 2022 are shown in Fig. 5a, together with a scatterplot between the total VCD and NS concentrations in Fig. 5b and 3-D plots of the vertical variation of lidar backscatter coefficients in Fig. 5c and Pandora-derived NO$_2$ concentrations in Fig. 5d. The observational data for 18 January reveal distinct diurnal patterns in NO$_2$ dynamics, with NS concentrations exhibiting higher baseline levels than those on 14 January, while following a similar initial decreasing trend until 11:30. Subsequently, NS concentrations demonstrated nonlinear growth, plateauing at 0.12 mg m^{-3} (about 1 h after 14:30) before further increasing to 0.16 mg m^{-3} by 21:00, attributed to combined rush-hour emissions and reduced photochemical dissipation. Concurrently, total vertical column density (VCD) displayed accelerated morning depletion (from 54 to 36 mg m^{-3} between

08:30 and 12:30), but, in contrast to the 14th, after 11:30, the total VCD of NO$_2$ concentrations continued to decrease while the NS NO$_2$ concentrations increased. Hence, in this situation, it may be difficult to determine NS NO$_2$ concentrations from the relationship ($R = 0.40$) before 13:00 (Fig 5b). After 13:00, the total VCD of NO$_2$ increased from about 37 mg m^{-2} to almost 60 mg m^{-2} at 16:30, with a plateau around 15:00, and the scatterplot in Fig. 5b shows a good correlation between TS and NS NO$_2$ concentrations.

The lidar data in Fig. 5c, with lower intensity than on 14 January, indicate smaller aerosol concentrations on 18 January than on 14 January, consistent with the smaller PM$_{2.5}$ concentrations (in Fig. 2b). The lidar data show the occurrence of multiple layers during the night and morning, with sharp boundaries indicating that aerosol particles are trapped in rather shallow layers with little or no exchange between these layers. After 10:30, the boundaries between layers became less sharp, indicating the onset of vertical transport, although the very shallow clear layer (dark blue) between 500 and 600 m indicates a clear separation between the lower and upper layers, prohibiting vertical transport. Around 13:00, this shallow layer disappeared, and after 15:00, the atmospheric boundary layer appeared well mixed up to the top at about 800 m.

The time series of the NO$_2$ vertical distributions in Fig. 5d shows that NO$_2$ concentrations were lower on the 18th than on the 14th and were concentrated below 1000 m. The observation of lower concentrations on the 18th and the 14th seems to be in contrast with the higher NS concentrations on the 18th than on the 14th mentioned above. However, the Pandora profiles are constructed from layer-averaged volume mixing ratios interpolated to six standard levels, and the lowest level is 0.2 km. Hence, in view of the layered structure on the 18th, the higher NS concentrations may be disconnected from the lowest layer set at 0.2 km. It is further noted that the Pandora vertical distributions show lower NO$_2$ concentrations on the 14th than on the 18th in the morning, whereas they are higher in the afternoon of the 14th. The NO$_2$ concentrations and their vertical distributions varied between 08:00 and 12:30, with an initial increase between 08:00 and 10:00, with a broad elevated maximum centered around 500 m, and another small maximum around 11:00. Apart from these, the NO$_2$ concentrations were rather homogeneously distributed up to the top of the atmospheric boundary layer at about 800 m, as also indicated by the lidar data. After about 12:00, the NO$_2$ concentrations increased with a significant enhancement after 14:00.

The evolution of the atmospheric boundary layer, as shown in detail by the lidar data, and the variation of the NO$_2$ concentration profiles provide a plausible explanation for the evolution of the total VCD and NS concentrations of NO$_2$ and their ratios, with changes around 11:30 and 13:00. The plateau in the NS NO$_2$ concentrations may be indicative of the dilution near the surface due to upward transport and ver-
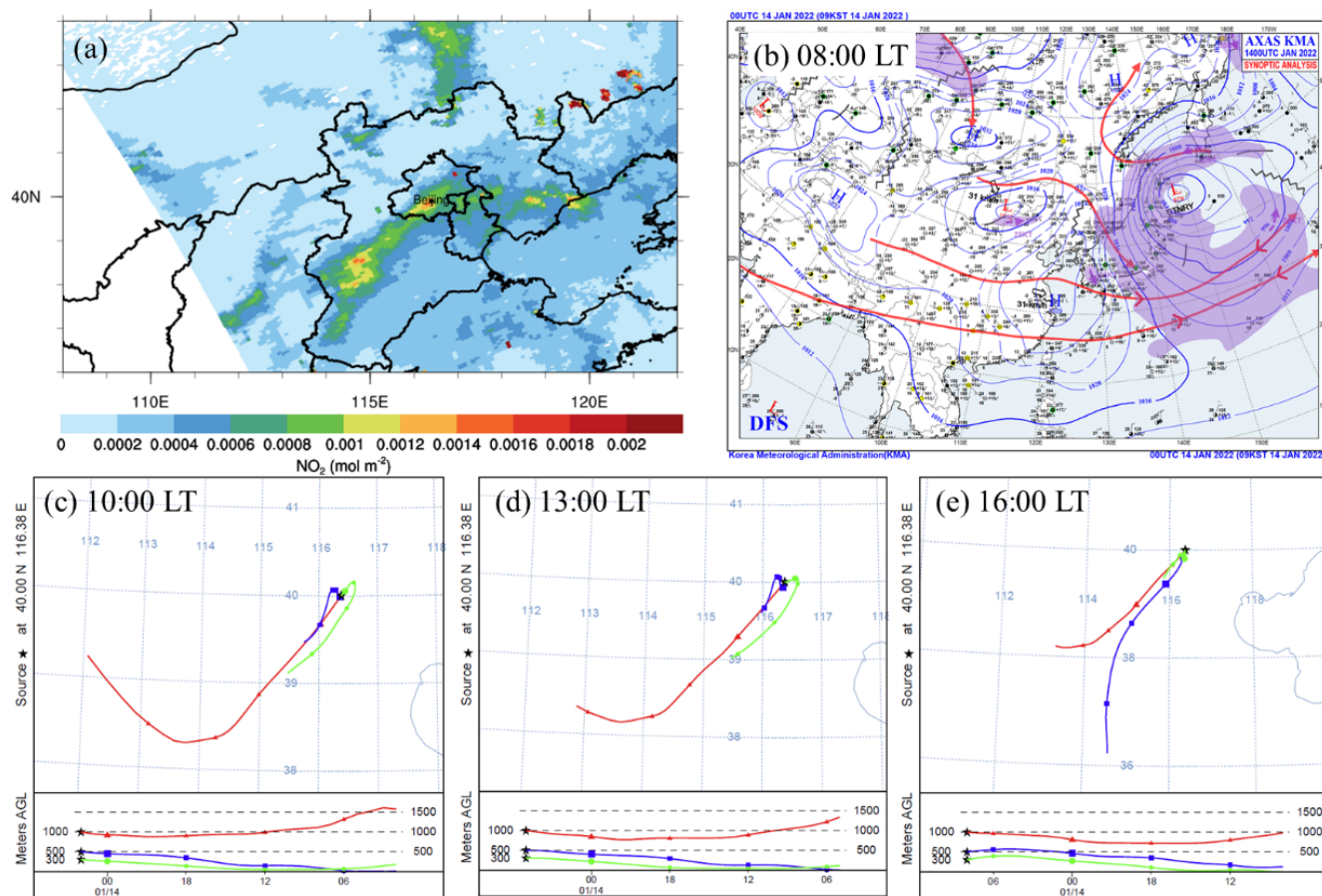
Figure 4. (a) Spatial distribution of tropospheric NO$_2$ in the study area derived from TROPOMI data on 14 January 2022. **(b)** Synoptic weather map at 00:00 UTC (08:00 LT); **(c–d)** 24 h backward air mass trajectories arriving at the Beijing-RADI site at 10:00 **(c)**, 13:00 **(d)**, and 16:00 LT **(e)** at heights of 300, 100, and 1000 m, calculated using the HYSPLIT model with 6 h time steps (00:00, 06:00, 12:00, and 18:00) and a shorter time step up to the arrival time.

tical mixing, at the same time increasing the TS NO$_2$ concentrations.

Figure 6 shows the large-scale situation for the study area on 18 January. The TROPOMI data in Fig. 6a show the spatial distribution of the tropospheric NO$_2$ VCDs, which are highest to the SE of Beijing, in Hebei/Tianjin and over the Yellow Sea. Over Beijing, the tropospheric NO$_2$ VCDs, as indicated by TROPOMI, are substantially lower than in case 1. This can be explained by the transport from clean areas to the west and west-northwest of Beijing, as indicated by the air mass trajectories arriving in Beijing at 300, 500, and 1000 m at 10:00, 13:00, and 16:00 LT (Fig. 6c). The trajectories of the air masses arriving at 10:00 LT show a clear difference between the lower and higher layers visible in the lidar data: the air arriving at 1000 m originated from the WNW and had traveled during the last 24 h over clean areas (Fig. 6a) over a distance of 1000 km (10°), between heights of 1000–1500 m, while the lower air mass was influenced by local air from SSW (at 300 m) and SW (500 m) that had traveled during the last 24 h near the surface at heights up to 500 m

over moderately polluted areas. Hence, the lidar data show higher aerosol content in the lower layer (< 500 m) than in the layer above (> 600 m), and both disconnected layers originated from different origins.

This situation changed as indicated by the air mass trajectory arriving at 13:00 LT. The air mass arriving at 300 m had the same characteristics as at 10:00 LT, had traveled an even shorter distance, and the layer adjacent to the surface was more stagnant. However, the air mass arriving at 500 m now came from the west, had traveled over clean areas (Fig. 6a) at heights between 500 and 1000 m, and thus was distinctly different from the layer below. The air mass arriving at 1000 m originated from a bit further north and further away (in Inner Mongolia) than at 10:00 LT and had traveled at heights between 750 and 1000 m. Hence, all three air masses suggest that the layers originated from different regions and likely had different compositions.

The trajectories of the air masses arriving at 16:00 LT indicate that the situation had changed, i.e., the pollution episode was finished, and pollution was replaced with cleaner air
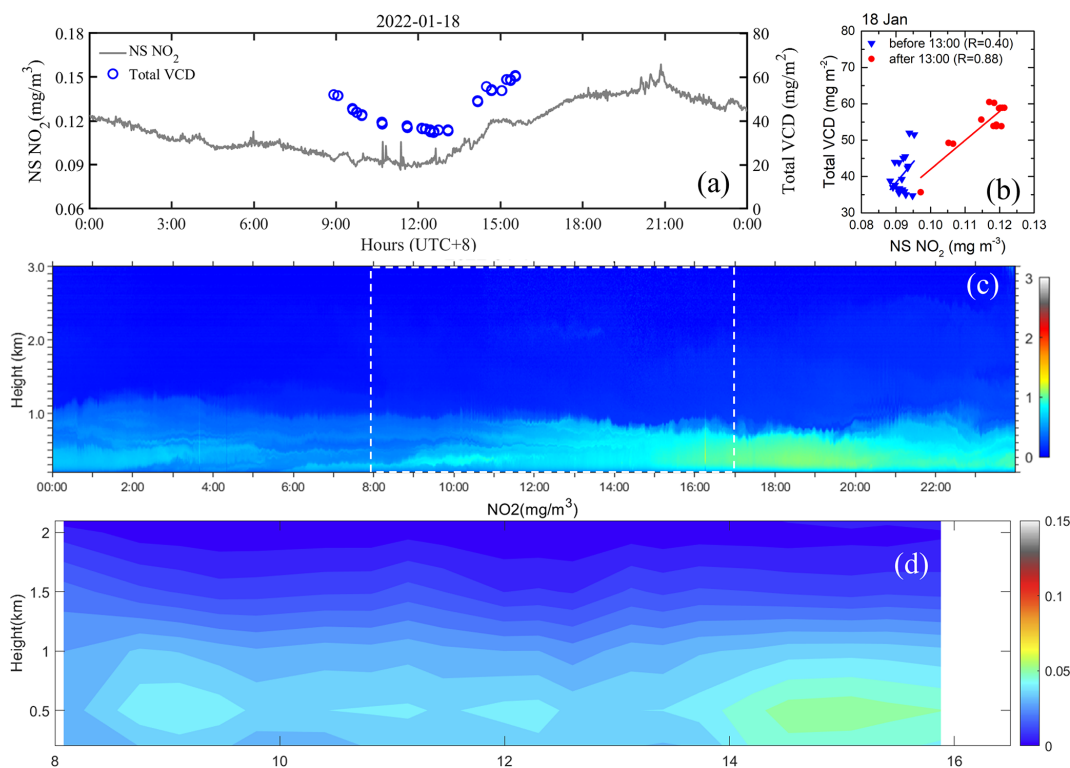
Figure 5. Same as Fig. 3 but for 18 January 2022.

transported from the W to WNW over distances of hundreds of km, originating from elevations of 500–1000 m for air masses arriving at 300 and 500 m, whereas the air mass arriving at 1000 m had actually followed a lower trajectory.

A comparative analysis of the two cases reveals distinct characteristics. Case 1, on 14 January, is characterized by a belt-shaped pollution event. The air mass arriving at 1000 m was primarily transported from Shanxi to Beijing, arriving from the SW during the last 15 h (Fig. 4c), while at lower levels the air masses traveled at low altitudes (from near the surface to 500 m) through the polluted area in Hebei (compare Fig. 4a and c). In contrast, case 2, on 18 January, was a large-scale pollution event covering Shandong, Hebei, Henan, and the southern part of Beijing (Fig. 6a), but the air mass arriving at 1000 m had been transported from the WNW over a large distance over clean areas. However, at lower levels, the air was stagnant (wind speed was low) in the morning; air masses arriving at 300 and 500 m at 10:00 LT had traveled over very short distances during the last 24 h and were thus only influenced by local pollution. In case 1, elevated pollutant concentrations were recorded in the 800–1000 m altitude layer in the morning, attributable to an air mass originating from Shanxi Province (with no significant pollution observed there) that was transported over the polluted area in Hebei at about 1000 m (Fig. 4a and c), and the upper-level air mass likely carried pollutant residuals that had been uplifted through vertical mixing processes over the polluted

area in Hebei. These pollutants were subsequently advected to Beijing, where their presence was detected by lidar observations. Conversely, in case 2, pollutants were predominantly transported from the plains, leading to a significant accumulation of pollutants in the near-surface layer. After 13:00, in both cases, the distinction between the pollutant layers disappeared when the boundary layers developed under the influence of surface heating and increasing wind speed (Fig. 2), thus creating boundary layer turbulence and mixing of NO_2, aerosols, and other constituents. Both the total VCD and NS concentrations of NO_2 increased, with that of total VCD of NO_2 being more significant. This further suggests that it is more difficult to obtain NS NO_2 concentrations using total VCD of NO_2 concentrations during the morning hours. However, utilizing the types of pollution spatial distribution and transport patterns can be helpful in indicating NS NO_2 concentrations.

3.3   Ratio of total VCD versus NS NO_2

The two pollution cases discussed above show that the ratio between total VCD and NS concentrations of NO_2 in the morning (before 13:00) is different from that in the afternoon (after 13:00) during the study period in the winter in Beijing. In order to better understand the relationship between total VCD and NS concentrations of NO_2, we calculated their ratio for each day, while we also differentiated between the
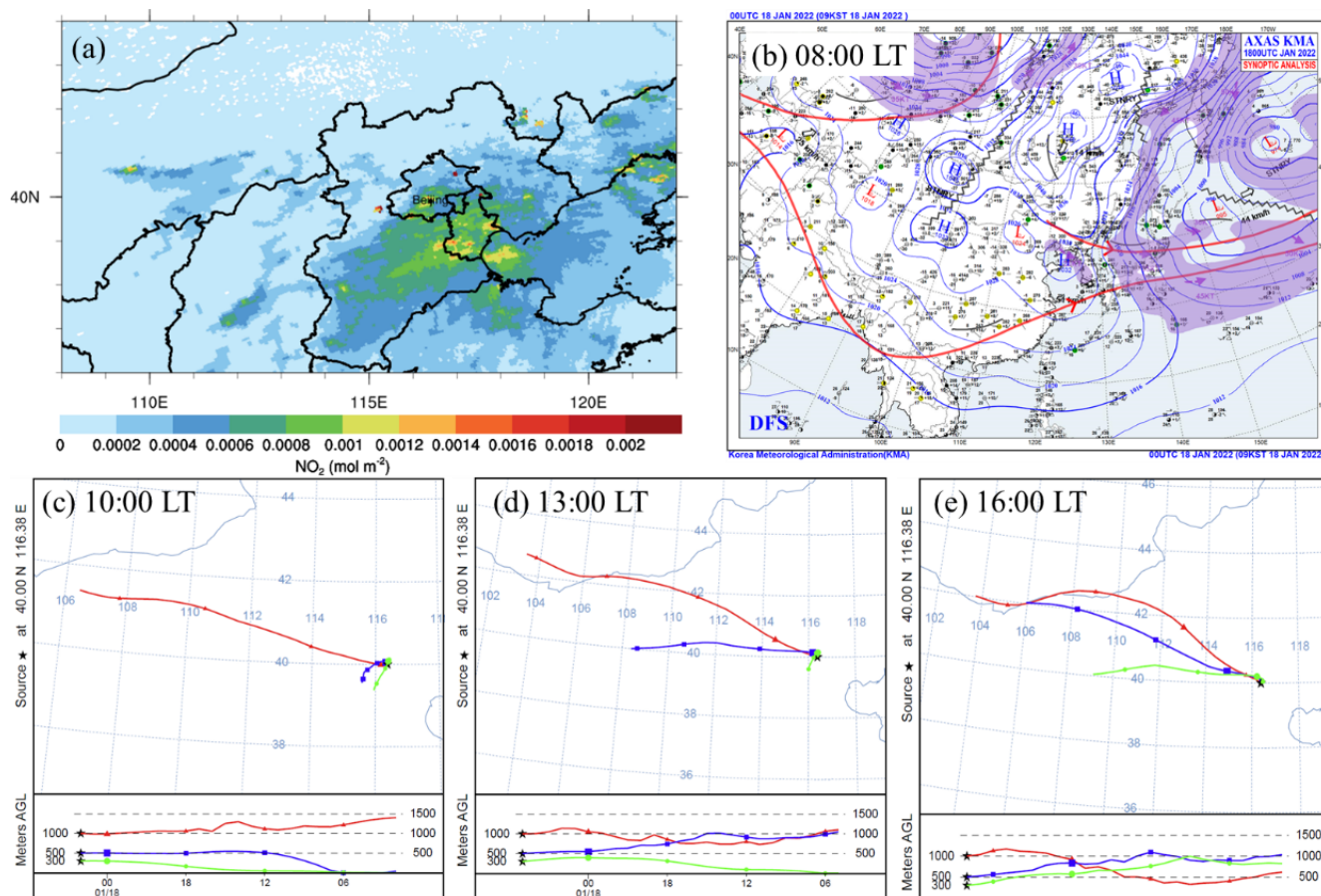
Figure 6. Same as Fig. 4 but for 18 January 2022.

morning and afternoon using 13:00 as the split time. The ratio of total VCD to NS NO$_2$ concentrations serves a dual purpose: it not only quantifies the changes between total VCD and NS concentrations of NO$_2$ when the correlation is low but also reflects the degree of dispersion between the two measurements. A more variable ratio indicates higher dispersion and poorer correlation, providing a straightforward yet effective way to assess the reliability of using total VCD of NO$_2$ to predict NS NO$_2$ concentrations.

The results are presented as violin plots in Fig. 7, for each of the 12 d for which data are available. The data in Fig. 7 show that the mean and median values of the NO$_2$ ratio during Period I (10–18 January) were substantially higher than those during Period III (25–30 January), with the exception of 25 and 29 January. These 2 d, at the beginning and end of Period III, signify the transition from polluted to clean days (see Fig. 2b). On most days, the ratio was smaller in the morning than in the afternoon. The difference between the morning and afternoon ratios was small during the 2 d (14th and 18th) with accumulated pollution, while during the 4 d, when wind speed increased on 13th, 15th, and 17th, the differences were relatively large, with the largest difference of 192 m on the 13th. During Period III, the difference between

the morning and afternoon ratios was basically smaller than 50 m, with a gap of more than 100 m only on the 29th. There were no valid observations of total VCD of NO$_2$ during Period II, so it is not possible to judge the changes in ratio over multiple consecutive days of pollution. Throughout the observation period, the standard deviations of the ratios were overall larger in the morning than in the afternoon, when the winter boundary layer was well mixed and the relationship between total VCD and NS concentrations of NO$_2$ was relatively stable. However, in the morning, when the boundary layer was developing, the day-to-day variations in the standard deviation imply relatively large changes in the ratio. The box plot in Fig. 7b illustrates the difference between the morning and afternoon ratios. The mean values are lower in the morning (364 m) than in the afternoon (428 m), and the upper quartile in the afternoon is closer to its median value, suggesting that the ratio is more stable in the afternoon when it is well mixed vertically. However, although the ratio is quite stable in the afternoon when the boundary layer is generally well mixed, there are still unpredictable extreme values (e.g., 771 m).

Generally, the temporal stability of the ratio is important. The ratio is overall less variable after 13:00, suggesting that
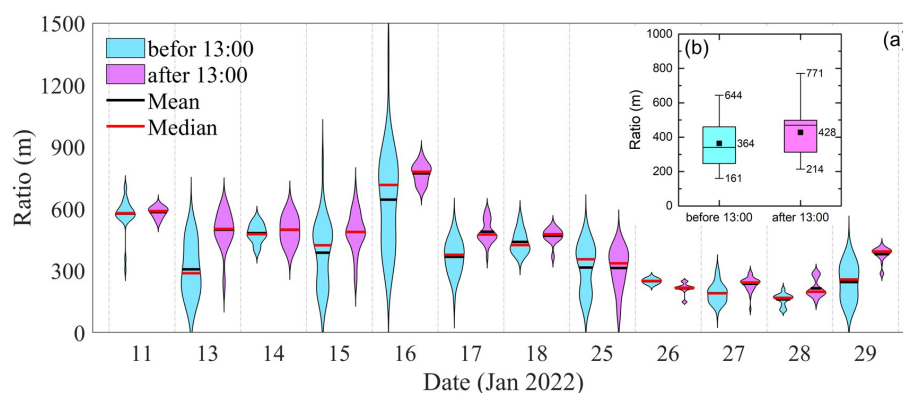
Figure 7. (a) Violin plots of the ratio of total VCD and NS concentrations of NO$_2$ for each day when observations were available in January 2022, where the data were differentiated between the morning (before 13:00 LT) and the afternoon (after 13:00 LT). **(b)** The box-whisker plot of the ratio averaged over all observations before and after 13:00 LT in January 2022. The horizontal lines in the boxes and the top and bottom edges represent the mean and upper and lower quartile values of the ratio, respectively; the solid square dots represent the median values, and the bars represent the minimum and maximum values.

polar-orbiting satellites can be used to predict NS NO$_2$ based on total VCD of NO$_2$ during this period with greater confidence. This temporal stability is particularly valuable because it offers a feasible approach for air quality monitoring and forecasting. In contrast, the ratio is less stable before 13:00, posing greater challenges for using geostationary satellites for the same prediction task. It is worth noting that our analysis of winter in Beijing suggests that considering both the spatial distribution of pollutants and their transport direction has the potential to enhance the ability of satellites to predict NS NO$_2$ concentrations based on total VCD of NO$_2$. By incorporating this information into prediction models, the accuracy and reliability of satellite-based air quality predictions may be improved, particularly in complex urban environments where pollutant concentrations can vary significantly over short distances and time periods.

4 Discussion and conclusions

Total column and near-surface NO$_2$ data observed during the winter field experiment from 10 to 29 January 2022 at the Beijing-RADI site were analyzed together with lidar, PM$_{2.5}$ and meteorological data, satellite data, weather maps, and air mass trajectories. Based on these observations, the experimental period was subdivided into three periods: intermittent pollution days, persistent pollution days, and clean days. The analysis of the total VCD and NS concentrations of NO$_2$ shows substantial differences between the first and third periods, while during the second period, with persistent pollution, no total VCD of NO$_2$ observations were available due to the presence of clouds. During the first period, two episodes with high pollution were identified and analyzed in detail with a focus on the ratio between the variation of the total VCD and NS concentrations of NO$_2$ and their ratio. The relations between the total VCD and NS concentrations of

NO$_2$ in the morning and in the afternoon, split at 13:00 LT, appear to be significantly different. These differences have been explained in terms of boundary layer dynamics, using lidar data showing the vertical stratification with disconnected boundary layers at different heights in the morning, which connected as the boundary layer developed in the afternoon. In addition, the four-layer NO$_2$ column concentrations obtained from Pandora show good agreement with the lidar signal in terms of the temporal and vertical variations of the NO$_2$ concentrations, with differences attributed to the different vertical resolutions of the Pandora and lidar observations, as well as the physical properties of NO$_2$ and aerosols. From this, together with air mass trajectories, weather maps, and TROPOMI satellite observations of the NO$_2$ spatial distribution, a consistent picture was created showing different source regions for disconnected air masses arriving at different heights and different times of the day.

Data from the full experimental period, with 12 d for which valid data are available, were analyzed in detail to obtain more insight into the variation of the ratio between the total VCD and NS concentrations of NO$_2$. This ratio appears to be overall smaller in the morning than in the afternoon, with larger standard deviations. In addition, the ratios and their standard deviations were overall larger during the more polluted episode I than during the relatively clean Period III.

Daytime continuous remote sensing observations of Pandora were used in this study, and the results confirm its possible importance in understanding changes in the distribution of NO$_2$ in the vertical direction. The NO$_2$ vertical distribution has been analyzed using less than 3 weeks of observation data, which has some limitations, but the research idea is worthy of reference and promotion. In the future, the implementation of larger-scale experiments in different typical regions and seasons will help to provide further understanding of the ideas presented in this study and improve the

shortcomings. Moreover, we will broaden the scope of experimental areas and field sites to complement research on the various pollutant emission and transport characteristics. Furthermore, observations over a longer period will allow us to capture more representative cases, thereby enhancing the reliability of our findings.

The overall conclusion from this study during a relatively short period of almost 3 weeks in the winter in Beijing is that the variation between the total column and near-surface NO$_2$ concentrations varies with the concentration level and the time of day. In the afternoon, the boundary layer is well developed and satellite observations are sensitive to the NS concentrations, whereas in the morning this depends on meteorological conditions. Hence, satellites with an afternoon overpass are capable of measuring total VCD of NO$_2$ that is representative of NS concentrations, whereas observations earlier in the day may not be. This could possibly affect the interpretation of diurnal variations derived from observations using geostationary satellites.

Author contributions. YZ and YW conceived and designed the study. OL processed the Pandora data. YC collected and processed the meteorological data. YL processed the lidar data. YZ and GL prepared the paper with contributions from all coauthors. Y-XZ and ZL provided project funding.

References

Atkinson, R.: Atmospheric chemistry of VOCs and NO$_x$, Atmos. Environ., 34, 2063–2101, https://doi.org/10.1016/S1352-2310(99)00460-4, 2000.

Boersma, K. F., Jacob, D. J., Trainic, M., Rudich, Y., DeSmedt, I., Dirksen, R., and Eskes, H. J.: Validation of urban NO$_2$ concentrations and their diurnal and seasonal variations observed from the SCIAMACHY and OMI sensors using in situ surface measurements in Israeli cities, Atmos. Chem. Phys., 9, 3867–3879, https://doi.org/10.5194/acp-9-3867-2009, 2009.

Cede, A.: Manual for Blick Software Suite 1.8; Manual version 1.8-5, 14 Aug 2024, 202 pp., https://www.pandonia-global-network.org/wp-content/uploads/2024/08/BlickSoftwareSuite_Manual_v1-8-5.pdf (last access: 21 January, 2025), 2024.

Chang, B., Liu, H., Zhang, C., Xing, C., Tan, W., and Liu, C.: Relating satellite NO$_2$ tropospheric columns to near-surface concentrations: implications from ground-based MAX-DOAS NO$_2$ vertical profile observations, npj Climate and Atmospheric Science, 8, 1, https://doi.org/10.1038/s41612-024-00891-z, 2025.

Chang, L.-S., Kim, D., Hong, H., Kim, D.-R., Yu, J.-A., Lee, K., Lee, H., Kim, D., Hong, J., Jo, H.-Y., and Kim, C.-H.: Evaluation of correlated Pandora column NO$_2$ and in situ surface NO$_2$ measurements during GMAP campaign, Atmos. Chem. Phys., 22, 10703–10720, https://doi.org/10.5194/acp-22-10703-2022, 2022.

Chang, X., Wang, S., Zhao, B., Xing, J., Liu, X., Wei, L., Song, Y., Wu, W., Cai, S., Zheng, H., Ding, D., and Zheng, M.: Contributions of inter-city and regional transport to PM$_{2.5}$ concentrations in the Beijing-Tianjin-Hebei region and its implications on regional joint air pollution control, Sci. Total Environ., 660, 1191–1200, https://doi.org/10.1016/j.scitotenv.2018.12.474, 2019.

Cheng, N., Li, Y., Sun, F., Chen, C., Wang, B., Li, Q., Wei, P., and Cheng, B.: Ground-Level NO$_2$ in Urban Beijing: Trends, Distribution, and Effects of Emission Reduction Measures, Aerosol Air Qual. Res., 18, 343–356, https://doi.org/10.4209/aaqr.2017.02.0092, 2018.

de Leeuw, G., van der A, R., Bai, J., Xue, Y., Varotsos, C., Li, Z., Fan, C., Chen, X., Christodoulakis, I., Ding, J., Hou, X., Kouremadas, G., Li, D., Wang, J., Zara, M., Zhang, K., and Zhang, Y.: Air Quality over China, Remote Sens., 13, 3542, https://doi.org/10.3390/rs13173542, 2021.

de Souza, A., Aristone, F., Abreu, M. C., de Oliveira-Júnior, J. F., Fernandes, W. A., and Pobocikova, I.: Spatio-temporal variations of tropospheric nitrogen dioxide in South Mato Grosso based on remote sensing by satellite, Meteorol. Atmos. Phys., 134, 19, https://doi.org/10.1007/s00703-021-00855-5, 2022.

Ding, J., van der A, R. J., Mijling, B., Jalkanen, J.-P., Johansson, L., and Levelt, P. F.: Maritime NO$_x$ Emissions Over Chinese Seas Derived From Satellite Observations, Geophys. Res. Lett., 45, 2031–2037, https://doi.org/10.1002/2017GL076788, 2018.

Dong, Z., Wang, S., Xing, J., Chang, X., Ding, D., and Zheng, H.: Regional transport in Beijing-Tianjin-Hebei region and its changes during 2014–2017: The impacts of meteorology and emission reduction, Sci. Total Environ., 737, 139792, https://doi.org/10.1016/j.scitotenv.2020.139792, 2020.

Dou, X., Liao, C., Wang, H., Huang, Y., Tu, Y., Huang, X., Peng, Y., Zhu, B., Tan, J., Deng, Z., Wu, N., Sun, T., Ke, P., and Liu, Z.: Estimates of daily ground-level NO$_2$ concentrations in China based on Random Forest model integrated K-means, Advances in Applied Energy, 2, 100017, https://doi.org/10.1016/j.adapen.2021.100017, 2021.

Draxler, R. R. and Hess, G. D.: An Overview of the HYSPLIT_4 Modelling System for Trajectories, Dispersion, and Deposition, https://www.arl.noaa.gov/documents/reports/MetMag.pdf (last access: 25 April 2025), 1998.

Duncan, B. N., Lamsal, L. N., Thompson, A. M., Yoshida, Y., Lu, Z., Streets, D. G., Hurwitz, M. M., and Pickering, K. E.: A space-based, high-resolution view of notable changes in urban NO$_x$ pollution around the world (2005–2014), J. Geophys. Res.-Atmos., 121, 976–996, https://doi.org/10.1002/2015JD024121, 2016.

Eum, K.-D., Kazemiparkouhi, F., Wang, B., Manjourides, J., Pun, V., Pavlu, V., and Suh, H.: Long-term NO$_2$ exposures and cause-specific mortality in American older adults, Environ. Int., 124, 10–15, https://doi.org/10.1016/j.envint.2018.12.060, 2019.

Eum, K.-D., Honda, T. J., Wang, B., Kazemiparkouhi, F., Manjourides, J., Pun, V. C., Pavlu, V., and Suh, H.: Long-term nitrogen dioxide exposure and cause-specific mortality in the U.S. Medicare population, Environ. Res., 207, 112154, https://doi.org/10.1016/j.envres.2021.112154, 2022.

Fan, C., Li, Z., Li, Y., Dong, J., van der A, R., and de Leeuw, G.: Variability of NO$_2$ concentrations over China and effect on air quality derived from satellite and ground-based observations, Atmos. Chem. Phys., 21, 7723–7748, https://doi.org/10.5194/acp-21-7723-2021, 2021.

Flynn, C. M., Pickering, K. E., Crawford, J. H., Lamsal, L., Krotkov, N., Herman, J., Weinheimer, A., Chen, G., Liu, X., Szykman, J., Tsay, S.-C., Loughner, C., Hains, J., Lee, P., Dickerson, R. R., Stehr, J. W., and Brent, L.: Relationship between column-density and surface mixing ratio: Statistical analysis of O$_3$ and NO$_2$ data from the July 2011 Maryland DISCOVER-AQ mission, Atmos. Environ., 92, 429–441, https://doi.org/10.1016/j.atmosenv.2014.04.041, 2014.

Goldberg, D. L., Anenberg, S. C., Kerr, G. H., Mohegh, A., Lu, Z., and Streets, D. G.: TROPOMI NO$_2$ in the United States: A Detailed Look at the Annual Averages, Weekly Cycles, Effects of Temperature, and Correlation With Surface NO$_2$ Concentrations, Earth's Future, 9, e2020EF001665, https://doi.org/10.1029/2020EF001665, 2021.

Herman, J., Cede, A., Spinei, E., Mount, G., Tzortziou, M., and Abuhassan, N.: NO$_2$ column amounts from ground-based Pandora and MFDOAS spectrometers using the direct-sun DOAS technique: Intercomparisons and application to OMI validation, J. Geophys. Res.-Atmos., 114, D13307, https://doi.org/10.1029/2009JD011848, 2009.

Herman, J., Abuhassan, N., Kim, J., Kim, J., Dubey, M., Raponi, M., and Tzortziou, M.: Underestimation of column NO$_2$ amounts from the OMI satellite compared to diurnally varying ground-based retrievals from multiple PANDORA spectrometer instruments, Atmos. Meas. Tech., 12, 5593–5612, https://doi.org/10.5194/amt-12-5593-2019, 2019.

Huang, X., Yang, K., Kondragunta, S., Wei, Z., Valin, L., Szykman, J., and Goldberg, M.: NO$_2$ retrievals from NOAA-20 OMPS: Algorithm, evaluation, and observations of drastic changes during COVID-19, Atmos. Environ., 290, 119367, https://doi.org/10.1016/j.atmosenv.2022.119367, 2022.

Ialongo, I., Virta, H., Eskes, H., Hovila, J., and Douros, J.: Comparison of TROPOMI/Sentinel-5 Precursor NO$_2$ observations with ground-based measurements in Helsinki, Atmos. Meas. Tech., 13, 205–218, https://doi.org/10.5194/amt-13-205-2020, 2020.

Kang, Y., Tang, G., Li, Q., Liu, B., Cao, J., Hu, Q., and Wang, Y.: Evaluation and Evolution of MAX-DOAS-observed Vertical NO$_2$ Profiles in Urban Beijing, Adv. Atmos. Sci., 38, 1188–1196, https://doi.org/10.1007/s00376-021-0370-1, 2021.

Kim, J., Jeong, U., Ahn, M.-H., et al.: New Era of Air Quality Monitoring from Space: Geostationary Environment Monitoring Spectrometer (GEMS), B. Am. Meteorol. Soc., 101, E1–E22, https://doi.org/10.1175/BAMS-D-18-0013.1, 2020.

Knepp, T., Pippin, M., Crawford, J., Chen, G., Szykman, J., Long, R., Cowen, L., Cede, A., Abuhassan, N., Herman, J., Delgado, R., Compton, J., Berkoff, T., Fishman, J., Martins, D., Stauffer, R., Thompson, A. M., Weinheimer, A., Knapp, D., Montzka, D., Lenschow, D., and Neil, D.: Estimating surface NO$_2$ and SO$_2$ mixing ratios from fast-response total column observations and potential application to geostationary missions, J. Atmos. Chem., 72, 261–286, https://doi.org/10.1007/s10874-013-9257-6, 2015.

KNMI: Algorithm theoretical basis document for the TROPOMI L01b data processor, Tech. Rep. S5P-KNMI-L01B 0009-SD, Koninklijk Nederlands Meteorologisch Instituut (KNMI), CI-6480-ATBD, issue 8.0.0, https://sentinels.copernicus.eu/documents/247904/2476257/Sentinel-5P-TROPOMI-Level-1B-ATBD (last access: 11 January 2020), 2017.

Kornartit, C., Sokhi, R. S., Burton, M. A., and Ravindra, K.: Activity pattern and personal exposure to nitrogen dioxide in indoor and outdoor microenvironments, Environ. Int., 36, 36–45, https://doi.org/10.1016/j.envint.2009.09.004, 2010.

Lamsal, L. N., Krotkov, N. A., Celarier, E. A., Swartz, W. H., Pickering, K. E., Bucsela, E. J., Gleason, J. F., Martin, R. V., Philip, S., Irie, H., Cede, A., Herman, J., Weinheimer, A., Szykman, J. J., and Knepp, T. N.: Evaluation of OMI operational standard NO$_2$ column retrievals using in situ and surface-based NO$_2$ observations, Atmos. Chem. Phys., 14, 11587–11609, https://doi.org/10.5194/acp-14-11587-2014, 2014.

Levelt, P. F., Oord, G. H. J. v. d., Dobber, M. R., Malkki, A., Huib, V., Johan de, V., Stammes, P., Lundell, J. O. V., and Saari, H.: The ozone monitoring instrument, IEEE T. Geosci. Remote, 44, 1093–1101, https://doi.org/10.1109/TGRS.2006.872333, 2006.

Li, D., Liu, J., Zhang, J., Gui, H., Du, P., Yu, T., Wang, J., Lu, Y., Liu, W., and Cheng, Y.: Identification of long-range transport pathways and potential sources of PM$_{2.5}$ and PM$_{10}$ in Beijing from 2014 to 2015, J. Environ. Sci., 56, 214–229, https://doi.org/10.1016/j.jes.2016.06.035, 2017.

Li, J., Wang, Y., Zhang, R., Smeltzer, C., Weinheimer, A., Herman, J., Boersma, K. F., Celarier, E. A., Long, R. W., Szykman, J. J., Delgado, R., Thompson, A. M., Knepp, T. N., Lamsal, L. N., Janz, S. J., Kowalewski, M. G., Liu, X., and Nowlan, C. R.: Comprehensive evaluations of diurnal NO$_2$ measurements during DISCOVER-AQ 2011: effects of resolution-dependent representation of NO$_x$ emissions, Atmos. Chem. Phys., 21, 11133–11160, https://doi.org/10.5194/acp-21-11133-2021, 2021.

Liu, O., Li, Z., Lin, Y., Fan, C., Zhang, Y., Li, K., Zhang, P., Wei, Y., Chen, T., Dong, J., and de Leeuw, G.: Evaluation of the first

year of Pandora NO$_2$ measurements over Beijing and application to satellite validation, Atmos. Meas. Tech., 17, 377–395, https://doi.org/10.5194/amt-17-377-2024, 2024.

Nordeide Kuiper, I., Svanes, C., Markevych, I., Accordini, S., Bertelsen, R. J., Bråbäck, L., Heile Christensen, J., Forsberg, B., Halvorsen, T., Heinrich, J., Hertel, O., Hoek, G., Holm, M., de Hoogh, K., Janson, C., Malinovschi, A., Marcon, A., Miodini Nilsen, R., Sigsgaard, T., and Johannessen, A.: Lifelong exposure to air pollution and greenness in relation to asthma, rhinitis and lung function in adulthood, Environ. Int., 146, 106219, https://doi.org/10.1016/j.envint.2020.106219, 2021.

Reed, A. J., Thompson, A. M., Kollonige, D. E., Martins, D. K., Tzortziou, M. A., Herman, J. R., Berkoff, T. A., Abuhassan, N. K., and Cede, A.: Effects of local meteorology and aerosols on ozone and nitrogen dioxide retrievals from OMI and pandora spectrometers in Maryland, USA during DISCOVER-AQ 2011, J. Atmos. Chem., 72, 455–482, https://doi.org/10.1007/s10874-013-9254-9, 2015.

Song, J., Zang, L., Mao, F., Zhang, Y., and Chen, J.: Hourly nearground NO$_2$ concentration retrieval from geostationary satellite observations, Int. Arch. Photogramm. Remote Sens. Spatial Inf. Sci., XLVIII-1-2024, 599–604, https://doi.org/10.5194/isprs-archives-XLVIII-1-2024-599-2024, 2024.

Stein, A. F., Draxler, R. R., Rolph, G. D., Stunder, B. J. B., Cohen, M. D., and Ngan, F.: NOAA's HYSPLIT Atmospheric Transport and Dispersion Modeling System, B. Am. Meteorol. Soc., 96, 2059–2077, https://doi.org/10.1175/BAMS-D-14-00110.1, 2015.

Stull, R. B.: An Introduction to Boundary Layer Meteorology, Kluwer Academic Publishers, Dordrecht, The Netherlands, 666 pp., https://doi.org/10.1007/978-94-009-3027-8, ISBN 90-227-2768-6, 1988.

Sun, T., Zhang, T., Xiang, Y., Fan, G., Fu, Y., and Lv, L.: Investigation on the vertical distribution and transportation of PM$_{2.5}$ in the Beijing-Tianjin-Hebei region based on stereoscopic observation network, Atmos. Environ., 294, 119511, https://doi.org/10.1016/j.atmosenv.2022.119511, 2023.

Tang, T., Cheng, T., Zhu, H., Ye, X., Fan, D., Li, X., and Tong, H.: Quantifying instantaneous nitrogen oxides emissions from power plants based on space observations, Sci. Total Environ., 938, 173479, https://doi.org/10.1016/j.scitotenv.2024.173479, 2024.

Thompson, A. M., Stauffer, R. M., Boyle, T. P., Kollonige, D. E., Miyazaki, K., Tzortziou, M., Herman, J. R., Abuhassan, N., Jordan, C. E., and Lamb, B. T.: Comparison of Near-Surface NO$_2$ Pollution With Pandora Total Column NO$_2$ During the Korea-United States Ocean Color (KORUS OC) Campaign, J. Geophys. Res.-Atmos., 124, 13560–13575, https://doi.org/10.1029/2019JD030765, 2019.

Tzortziou, M., Herman, J. R., Cede, A., Loughner, C. P., Abuhassan, N., and Naik, S.: Spatial and temporal variability of ozone and nitrogen dioxide over a major urban estuarine ecosystem, J. Atmos. Chem., 72, 287–309, https://doi.org/10.1007/s10874-013-9255-8, 2015.

Tzortziou, M., Parker, O., Lamb, B., Herman, J. R., Lamsal, L., Stauffer, R., and Abuhassan, N.: Atmospheric Trace Gas (NO$_2$ and O$_3$) Variability in South Korean Coastal Waters, and Implications for Remote Sensing of Coastal Ocean Color Dynamics, Remote Sens., 10, 1587, https://doi.org/10.3390/rs10101587, 2018.

van der A, R. J., Peters, D. H. M. U., Eskes, H., Boersma, K. F., Van Roozendael, M., De Smedt, I., and Kelder, H. M.: Detection of the trend and seasonal variation in tropospheric NO$_2$ over China, J. Geophys. Res.-Atmos., 111, D12317, https://doi.org/10.1029/2005JD006594, 2006.

van der A, R. J., Mijling, B., Ding, J., Koukouli, M. E., Liu, F., Li, Q., Mao, H., and Theys, N.: Cleaning up the air: effectiveness of air quality policy for SO$_2$ and NO$_x$ emissions in China, Atmos. Chem. Phys., 17, 1775–1789, https://doi.org/10.5194/acp-17-1775-2017, 2017.

van Geffen, J. H. G. M., Boersma, K. F., Van Roozendael, M., Hendrick, F., Mahieu, E., De Smedt, I., Sneep, M., and Veefkind, J. P.: Improved spectral fitting of nitrogen dioxide from OMI in the 405–465 nm window, Atmos. Meas. Tech., 8, 1685–1699, https://doi.org/10.5194/amt-8-1685-2015, 2015.

van Geffen, J. H. G. M., Eskes, H. J., Boersma, K. F., Maasakkers, J. D., and Veefkind, J. P.: TROPOMI ATBD of the total and tropospheric NO$_2$ data products, Tech. Rep. S5P-KNMI-L2-0005-RP, Koninklijk Nederlands Meteorologisch Instituut (KNMI), CI-7430-ATBD, issue 1.4.0, https://sentinels.copernicus.eu/documents/247904/2476257/Sentinel-5P-TROPOMI-ATBD-NO2-data-products (last access: 11 January 2020), 2019.

Veefkind, J. P., Aben, I., McMullan, K., Förster, H., de Vries, J., Otter, G., Claas, J., Eskes, H. J., de Haan, J. F., Kleipool, Q., van Weele, M., Hasekamp, O., Hoogeveen, R., Landgraf, J., Snel, R., Tol, P., Ingmann, P., Voors, R., Kruizinga, B., Vink, R., Visser, H., and Levelt, P. F.: TROPOMI on the ESA Sentinel-5 Precursor: A GMES mission for global observations of the atmospheric composition for climate, air quality and ozone layer applications, Remote Sens. Environ., 120, 70–83, https://doi.org/10.1016/j.rse.2011.09.027, 2012.

Wei, J., Liu, S., Li, Z., Liu, C., Qin, K., Liu, X., Pinker, R. T., Dickerson, R. R., Lin, J., Boersma, K. F., Sun, L., Li, R., Xue, W., Cui, Y., Zhang, C., and Wang, J.: Ground-Level NO$_2$ Surveillance from Space Across China for High Resolution Using Interpretable Spatiotemporally Weighted Artificial Intelligence, Environ. Sci. Technol., 56, 9988–9998, https://doi.org/10.1021/acs.est.2c03834, 2022.

Xing, C., Liu, C., Wang, S., Chan, K. L., Gao, Y., Huang, X., Su, W., Zhang, C., Dong, Y., Fan, G., Zhang, T., Chen, Z., Hu, Q., Su, H., Xie, Z., and Liu, J.: Observations of the vertical distributions of summertime atmospheric pollutants and the corresponding ozone production in Shanghai, China, Atmos. Chem. Phys., 17, 14275–14289, https://doi.org/10.5194/acp-17-14275-2017, 2017.

Yin, D., Song, Q., Guo, Y., Jiang, Y., Dong, Z., Zhao, B., Wang, S., Gao, D., Chang, X., Zheng, H., Li, S., Li, Y., and Liu, B.: Regional transport characteristics of PM$_{2.5}$ pollution events in Beijing during 2018–2021, J. Environ. Sci., 152, 503–515, https://doi.org/10.1016/j.jes.2024.05.044, 2025.

Zhang, C., Liu, C., Li, B., Zhao, F., and Zhao, C.: Spatiotemporal neural network for estimating surface NO$_2$ concentrations over north China and their human health impact, Environ. Pollut., 307, 119510, https://doi.org/10.1016/j.envpol.2022.119510, 2022.

Zhang, T., Zhang, R., Zhong, J., Che, H., Wang, J., and Guo, L.: The vertical pollution structure reflected by aerosol optical properties in Beijing and its relation with meteorological conditions in the autumn and winter of 2017–2020, Atmos. Environ., 308, 119870, https://doi.org/10.1016/j.atmosenv.2023.119870, 2023.

Zhang, Y., Wang, Y., Chen, G., Smeltzer, C., Crawford, J., Olson, J., Szykman, J., Weinheimer, A. J., Knapp, D. J., Montzka, D. D., Wisthaler, A., Mikoviny, T., Fried, A., and Diskin, G.: Large vertical gradient of reactive nitrogen oxides in the boundary layer: Modeling analysis of DISCOVER-AQ 2011 observations, J. Geophys. Res.-Atmos., 121, 1922–1934, https://doi.org/10.1002/2015JD024203, 2016.

Zhao, X., Griffin, D., Fioletov, V., McLinden, C., Cede, A., Tiefengraber, M., Müller, M., Bognar, K., Strong, K., Boersma, F., Eskes, H., Davies, J., Ogyu, A., and Lee, S. C.: Assessment of the quality of TROPOMI high-spatial-resolution NO$_2$ data products in the Greater Toronto Area, Atmos. Meas. Tech., 13, 2131–2159, https://doi.org/10.5194/amt-13-2131-2020, 2020.

Zhao, Z., Lu, Y., Zhan, Y., Cheng, Y., Yang, F., Brook, J. R., and He, K.: Long-term spatiotemporal variations in surface NO$_2$ for Beijing reconstructed from surface data and satellite retrievals, Sci. Total Environ., 904, 166693, https://doi.org/10.1016/j.scitotenv.2023.166693, 2023.